J. Plasma Physics (2008), *vol.* 74, *part* 5, *pp.* 607–628. © 2008 Cambridge University Press
doi:10.1017/S0022377808007058 Printed in the United Kingdom

On nonlinear waves in Hall–MHD plasma

R. MITEVA and G. MANN

Astrophysikalisches Institut Potsdam, An der Sternwarte 16,
Potsdam, D-14482, Germany
(rmiteva@aip.de, gmann@aip.de)

(Received 26 July 2007 and accepted in revised form 27 November 2007, first published online 13 February 2008)

Abstract. Low-frequency magnetic field fluctuations are observed in space plasmas, e.g. as upstream waves at the Earth's bow shock. Such upstream waves can steepen into very large amplitude wave phenomena, e.g. short large-amplitude magnetic structures (or SLAMS for short), shocklets or discrete wave packets. Such observations motivated us to study the nonlinear behavior of low-frequency and large-amplitude plasma waves in terms of the full nonlinear Hall–MHD framework. In the case of stationary (nonlinear) waves, the Hall–MHD equations can be rewritten in the so-called Sakai–Sonnerup system of equations that describe this plasma state and provide oscillatory and solitary types of solutions. An overall parameter study on the polarization characteristics, together with the magnetic field components and density variations of the different ranges of solutions, is presented here. These results can be further on applied to the theoretical treatment of particle interaction with such waves, e.g. at shocks in space plasmas, possibly leading to particle acceleration.

1. Introduction

Nonlinear waves are already observed in different space plasma environments and also in terms of different wave-like structures. For example, large-amplitude magnetic field fluctuations are often observed by *in situ* measurements in space, e.g. at the Earth's bow shock (see Paschmann et al. 1979; Hoppe et al. 1981; Mann and Lühr 1991; Mann et al. 1994), at other planetary bow shocks (e.g. Fairfield and Behannon 1976; Hoppe and Russell 1981; Goldstein et al. 1983), in the vicinity of comets (e.g. Riedler et al. 1986; Tsurutani et al. 1987a,b), and at co-rotating interaction regions (CIRs) (e.g. Tsurutani et al. 1995). In general, all of these wave phenomena are thought to be generated by energetic particles produced at the related shocks (Paschmann et al. 1979). That is also confirmed by numerical simulations, as has been done in Akimoto et al. (1991) and Scholer et al. (1992).

An example of such magnetic field fluctuations are the so-called low-frequency upstream waves that appear, for instance, in the upstream region of the Earth's bow shock. Dual spacecraft measurements (e.g. Hoppe and Russell 1983) reveal that they have typical frequencies of 0.1 of the proton cyclotron frequency and amplitudes in the magnetic field fluctuations of 0.3 of the undisturbed magnetic field (e.g. Mann and Lühr 1991). They are correlated with density fluctuations (see Paschmann et al. 1979), i.e. they have been classified as fast magnetosonic waves.

Since the above-mentioned waves are compressive ones, they steepen into so-called shocklets, which are attached by magnetic field fluctuations with a higher

https://doi.org/10.1017/S0022377808007058 Published online by Cambridge University Press

frequency of about 10 times the frequency of the upstream waves (Mann and Lühr 1991). The dual spacecraft observations reveal that these are large-amplitude whistler waves with frequencies well above the proton cyclotron frequency (Hoppe and Russell 1983).

These upstream waves can steepen into very large amplitude wave phenomena, the so-called SLAMS, if they approach the shock (see Schwartz and Burgess 1991; Mann et al. 1994). They show magnetic field compression by a typical factor of about three and are also accompanied with density compression. Hence, a full nonlinear treatment is necessary.

All these phenomena seem to be closely related to each other and play an important role in the dynamics of the associated shock (see, e.g., Schwartz and Burgess 1991; Scholer 1993). These observations motivated us to study the nonlinear behavior of low-frequency plasma waves, without the intention of comparing the obtained theoretical results with the observed wave phenomena.

Since the frequency scale of these fluctuations is very much smaller than the electron plasma and electron cyclotron frequency, these phenomena are predominantly carried by the ions, whereas the electrons act as a neutralizing fluid. This allows us to consider a pure electron–proton plasma (i.e. two-fluid equations), neglecting the displacement current and the electron mass. When the electron mass is also neglected and a center of mass velocity of both fluids is introduced in the analysis, a further simplification of the theoretical approach is possible, namely in terms of the Hall–MHD theory (Huba 1995). The Hall term in the generalized Ohm's law allows this framework to explain phenomena with frequencies beyond the ion cyclotron frequency and a spatial extent of about the ion inertial length. Finally, we stress that, since the amplitude of the observed magnetic field fluctuations may be large (sometimes up to few times the magnitude of the undisturbed ambient magnetic field), a fully nonlinear description of the two-fluid equations is necessary, i.e. nonlinear terms cannot be neglected.

2. Basic equations

The system of equations used here for describing the plasma state was, for instance, presented by Sakai and Sonnerup (1983). The procedure for obtaining the so-called Sakai–Sonnerup system follows naturally from the system of Hall–MHD equations, where the usual assumptions have been made, namely, the displacement currents are neglected, isotropic and diagonal pressure tensors for the electrons and the protons are assumed, a quasi-neutral plasma state is considered, and finally the electrons are taken to be massless.

2.1. Hall–MHD equations

Thus, we start from the Hall–MHD system of equations (see, e.g., Huba 1995),

$$\frac{\partial N}{\partial t} + \nabla \cdot (N\mathbf{v}) = 0, \tag{2.1}$$

$$\frac{\partial \mathbf{v}}{\partial t} + (\mathbf{v} \cdot \nabla)\mathbf{v} = -\Gamma\beta_0 \frac{\nabla N}{N} + \frac{(\nabla \times \mathbf{B}) \times \mathbf{B}}{N}, \tag{2.2}$$

$$\frac{\partial \mathbf{B}}{\partial t} - \nabla \times (\mathbf{v} \times \mathbf{B}) = -\nabla \times \left[\frac{1}{N}(\nabla \times \mathbf{B}) \times \mathbf{B}\right], \tag{2.3}$$

https://doi.org/10.1017/S0022377808007058 Published online by Cambridge University Press

where $\Gamma = \gamma N^{(\gamma-1)}$, γ is the ratio of specific heats, N is the plasma number density, $\beta_0 = 8\pi N_0 k_B T/B^2$ is the plasma beta, N_0 is the background number density, k_B is the Boltzmann constant, T is the plasma temperature, and $\mathbf{B}$ is the plasma magnetic field. Additionally, the center of mass velocity $\mathbf{v} = (m_i\mathbf{v}_i + m_e\mathbf{v}_e)/(m_i + m_e)$ was introduced, with the ion velocity $\mathbf{v}_i$, the electron velocity $\mathbf{v}_e$, the ion mass m_i, and the electron mass m_e. The pressure term is taken to be $k_B T N_0 (N/N_0)^\gamma$.

In the above system of equations, normalization of the physical quantities has already been performed, namely $\mathbf{B}$ is normalized to B_0, N to N_0, $\mathbf{v}$ to the Alfvén speed $v_A = B_0/(4\pi m_i N_0)^{1/2}$, the time t to the inverse of the ion-cyclotron frequency ω_{ci}^{-1}, and ∇ and the wave number k to the inverse of the characteristic length of the system $L = c/\omega_{pi} \equiv v_A/\omega_{ci}$.

2.2. Sakai–Sonnerup system

When (2.1)–(2.3) are written by components, they constitute a system of normalized equations, henceforth called the Sakai–Sonnerup system, namely,

$$\frac{\partial N}{\partial t} + \frac{\partial}{\partial x}(Nu) = 0, \tag{2.4}$$

$$\frac{du}{dt} = -\Gamma\beta_0 \frac{1}{N}\frac{\partial N}{\partial x} - \frac{1}{2N}\left[\frac{\partial}{\partial x}(B_y^2 + B_z^2)\right], \tag{2.5}$$

$$\frac{dv_y}{dt} = \frac{1}{N} B_x \frac{\partial B_y}{\partial t}, \tag{2.6}$$

$$\frac{dv_z}{dt} = \frac{1}{N} B_x \frac{\partial B_z}{\partial t}, \tag{2.7}$$

$$\frac{dB_y}{dt} = -B_y \frac{\partial u}{\partial x} + B_x \frac{\partial v_y}{\partial x} + \frac{\partial}{\partial x}\left(\frac{B_x}{N}\frac{\partial B_z}{\partial x}\right), \tag{2.8}$$

$$\frac{dB_z}{dt} = -B_z \frac{\partial u}{\partial x} + B_x \frac{\partial v_z}{\partial x} - \frac{\partial}{\partial x}\left(\frac{B_x}{N}\frac{\partial B_y}{\partial x}\right), \tag{2.9}$$

with $v_x \equiv u$. Equations (2.4)–(2.9) represent the basic system of nonlinear equations that is to be studied.

2.3. Linear analysis

Initially, the usual linearization analysis is performed while assuming small-amplitude waves. In this sense, the background (undisturbed, denoted with subscript 0) state can be presented in the following dimensionless form:

$$N_0 = 1, \quad u_0 = v_{y0} = v_{z0} = 0, \quad B_{x0} = \cos\theta, \quad B_{y0} = 0, \quad B_{z0} = \sin\theta, \tag{2.10}$$

i.e. the (undisturbed) ambient magnetic field B_0 takes an angle θ to the x-axis. In general, the dimensionless quantities can be expressed as a sum of background and perturbed ones, namely,

$$N = 1 + n, \quad u = u_1, \quad v_y = v_{y1}, \quad v_z = v_{z1},$$

$$B_x = \cos\theta, \quad B_y = b_y, \quad B_z = b_z + \sin\theta. \tag{2.11}$$

Taking into account the relations (2.11) and performing the well-known plane wave analysis, namely, assuming that the perturbed quantities are proportional

https://doi.org/10.1017/S0022377808007058 Published online by Cambridge University Press

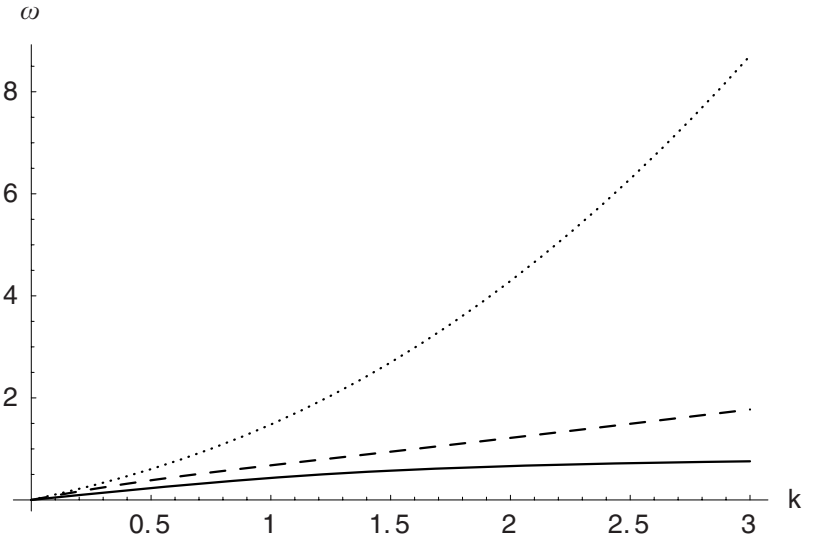


Figure 1. Plot of the linear dispersion relation (2.12) for $\beta_0 = 0.4$, $\gamma = 5/3$, and $\theta = 30°$, where the ion-cyclotron mode is represented by the solid curve, the sound mode by the dashed curve, and the whistler mode by the dotted curve.

to $\exp[i(kx - \omega t)]$, and hence $\partial/\partial t \to -i\omega$ and $\partial/\partial x \to ik$, one easily gets the dispersion relation for this plasma state from the determinant of the linearized system of equations, namely,

$$(\omega^2 - k^2 \cos^2\theta)\left[(\omega^2 - k^2\cos^2\theta) - \frac{\omega^2 k^2 \sin^2\theta}{\omega^2 - k^2\gamma\beta_0/2}\right] - \omega^2 k^4 \cos^2\theta = 0. \qquad (2.12)$$

When the above dispersion relation is plotted as a frequency–wave number dependency, one can recognize the ion-cyclotron, the sound, and the whistler wave modes, which are all plotted on Fig. 1. For small wave numbers, i.e. $k < 1$ (equivalent to $\omega < 1$), they degenerate to the well-known MHD modes: Alfvén (solid curve), slow (dashed curve), and fast magnetosonic mode (dotted curve).

3. Stationary solutions

When the amplitude of the wave is not small, the linearization analysis is no longer an appropriate description. Here, we search for stationary solutions of the Sakai–Sonnerup system (2.4)–(2.9), leading to solitary waves. Because in the present paper we look for a stationary solution, all functions need to be presented in the form

$$\xi = x - Vt, \qquad (3.1)$$

i.e. all varying quantities depend only on ξ and the new coordinate system is moving with the wave. Then,

$$\frac{\partial}{\partial t} = -V\frac{\partial}{\partial \xi} \quad \text{and} \quad \frac{\partial}{\partial x} = \frac{d}{d\xi}. \qquad (3.2)$$

Initially, a change of the coordinate systems is carried out, namely, each equation of the Sakai–Sonnerup system (2.4)–(2.9) is rewritten in a stationary system (moving with the same velocity V of the wave) or, equivalently, the relations (3.2) are taken

https://doi.org/10.1017/S0022377808007058 Published online by Cambridge University Press

into account. The system (2.4)–(2.9) becomes

$$-V\frac{dN}{d\xi}+\frac{d(Nu)}{d\xi}=0, \tag{3.3}$$

$$-V\frac{du}{d\xi}=-\frac{\gamma\beta_0}{2}N^{\gamma-1}\frac{dN}{d\xi}-\frac{1}{2}\frac{d(b_y^2+(b_z+\sin\theta)^2)}{d\xi}, \tag{3.4}$$

$$-V\frac{dv_y}{d\xi}=\cos\theta\frac{db_y}{d\xi}, \tag{3.5}$$

$$-V\frac{dv_z}{d\xi}=\cos\theta\frac{db_z}{d\xi}, \tag{3.6}$$

$$-V\frac{db_y}{d\xi}=\cos\theta\frac{dv_y}{d\xi}-\frac{d(ub_y)}{d\xi}+\frac{d}{d\xi}\left(\frac{\cos\theta}{N}\frac{db_z}{d\xi}\right), \tag{3.7}$$

$$-V\frac{db_z}{d\xi}=\cos\theta\frac{dv_z}{d\xi}-\frac{d(ub_z)}{d\xi}-\frac{d}{d\xi}\left(\frac{\cos\theta}{N}\frac{db_y}{d\xi}\right). \tag{3.8}$$

In this manner, all parameters depend only on ξ. Then, a spatial integration over ξ is performed, leading to the appearance of an integration constant for each of the six equations above. Each constant can now be fixed by means of the conditions (2.10), which define the undisturbed plasma state. Namely, the integrated equations for the plasma parameters are written for the undisturbed plasma state, fixing these constants. Additionally, in the case of solitary solutions, all disturbed quantities and their derivatives should vanish at infinity, i.e. $\xi\to\pm\infty$. In the case of oscillatory (or periodic) solutions, one should assume that b_y should be 0 at the maximum of b_z, i.e. at $db_z/d\xi=0$, as well as $b_z=0$ at the maximum of b_y, i.e. at $db_y/d\xi=0$. All these conditions lead to

$$C_1=-V,\quad C_2=\frac{\beta_0}{2}+\frac{\sin^2\theta}{2},\quad C_3=C_4=C_5=C_6=0, \tag{3.9}$$

for the integration constants of (3.3)–(3.8), respectively. Then, the so-obtained values of the integration constants are substituted back into the integrated equations.

Finally, the original system (3.3)–(3.8) can be reduced to the following system of equations:

$$\frac{b_y^2+b_z^2+2b_z\sin\theta}{2}=\frac{\beta_0}{2}(1-N^\gamma)+V^2\frac{N-1}{N}, \tag{3.10}$$

$$0=-\frac{\cos^2\theta}{V}b_y+\frac{V}{N}b_y+\frac{\cos\theta}{N}\frac{db_z}{d\xi}, \tag{3.11}$$

$$0=-\frac{\cos^2\theta}{V}b_z+\frac{V}{N}b_z-V\left(1-\frac{1}{N}\right)\sin\theta-\frac{\cos\theta}{N}\frac{db_y}{d\xi}. \tag{3.12}$$

This is the basic system of equations for our further study. It consists of one algebraic equation and two ordinary differential equations of first order. Note that the particle number density is a function of ξ, i.e. $N=N(\xi)$.

Because in the case of solitary solutions all disturbed quantities need to take small values at infinity, this justifies the linearization of (3.10)–(3.12) and the linearization

https://doi.org/10.1017/S0022377808007058 Published online by Cambridge University Press

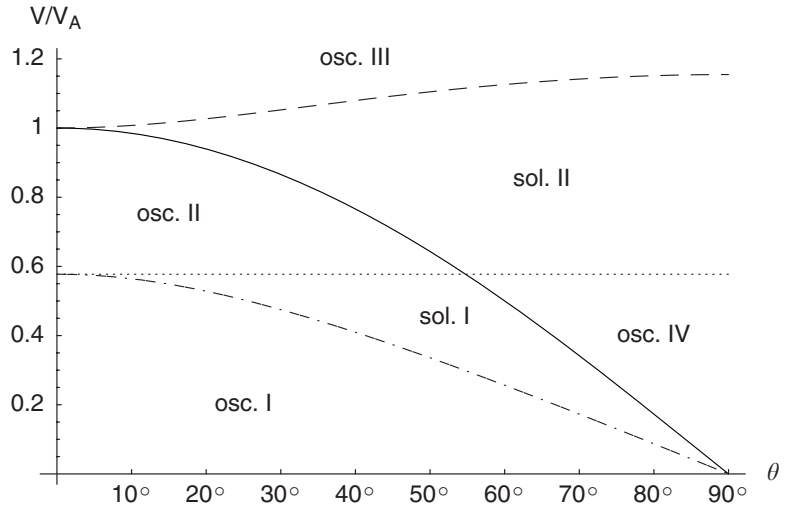


Figure 2. Plots of $V/V_{\rm A}$ as a function of the angle θ, where V_+ is denoted with a dashed curve, V_- with a dashed-dotted curve, $c_{\rm s}$ with a dotted curve, $\cos\theta$ with a solid curve and $\beta_0 = 0.4$ is also chosen.

gives

$$-\lambda^2 = \frac{(V^2 - \cos^2\theta)[(V^2 - V_+^2)(V^2 - V_-^2)]}{V^2\cos^2\theta(V^2 - c_{\rm s}^2)}, \tag{3.13}$$

where $V_\pm$ are the solutions of the equation $(V^2 - \cos^2\theta)(V^2 - c_{\rm s}^2) - V^2\sin^2\theta = 0$, namely,

$$V_\pm^2 = \frac{1 + c_{\rm s}^2}{2}\left[1 \pm \sqrt{1 - \frac{4c_{\rm s}^2\cos^2\theta}{(1 + c_{\rm s}^2)^2}}\right], \tag{3.14}$$

and $c_{\rm s} = (\gamma\beta_0/2)^{1/2}$ is the sound speed. Equation (3.13) contains two possibilities: (i) $-\lambda^2 < 0$ for solitary solutions, and (ii) $-\lambda^2 > 0$ for oscillatory solutions (waves). This gives the following ranges of solutions, as plotted on Fig. 2, where the ranges of solitary and oscillatory solutions are denoted by 'sol.' and 'osc.', respectively:

- $V < V_-, c_{\rm s}, \cos\theta, V_+$ or osc. I;
- $V_- < V < c_{\rm s}, \cos\theta, V_+$ or sol. I;
- $V_-, c_{\rm s} < V < \cos\theta, V_+$ or osc. II;
- $V_-, \cos\theta < V < c_{\rm s}, V_+$ or osc. IV;
- $V_-, c_{\rm s}, \cos\theta, < V < V_+$ or sol. II;
- $V_-, c_{\rm s}, \cos\theta, V_+ < V$ or osc. III.

Because here the kinetic effects are not taken into account, a low-beta plasma is assumed, namely $\beta_0 = 0.4$, and the fluid approach would be an appropriate plasma description. Thus, the only free parameters are the angle θ and the phase speed V. With the so-chosen parameters, some representative plots in each range of all possible solutions (oscillatory and solitary) can be computed. Note that the specific values of V and θ place the solutions in an oscillatory or in a solitary regime.

https://doi.org/10.1017/S0022377808007058 Published online by Cambridge University Press

Table 1. The parameter set and the computed $b_z(0)$ range, as used for the numerical calculation.

θ	V	$F(N_{\max})$	$N_{\max}$	Range of $b_z(0)$	Solution	Figure
0°	3	5.0159	3.441	(−3.167; 3.167)	Oscillatory	9, 11
0°	10	81.355	8.490	(−12.76; 12.76)	Oscillatory	9, 11
10°	0.7	0.0114	1.155	(−0.409; 0.057)	Oscillatory	3, 6
30°	0.2	0.0983	0.451	(−1.168; 0.168)	Oscillatory	2, 6
30°	0.55	0.0005	0.964	(−1.001; 0.001)	Solitary	12, 14
30°	0.7	0.1146	1.155	(−1.022; 0.022)	Oscillatory	3, 6
30°	0.86	0.0619	1.348	(−1.111; 0.111)	Oscillatory	8, 10
30°	1.0	0.1403	1.509	(−1.228; 0.228)	Solitary	13, 14
30°	1.6	0.853	2.148	(−1.898; 0.898)	Oscillatory	4, 7
60°	0.2	0.0983	0.451	(−1.839; 0.107)	Oscillatory	2, 6
60°	0.4	0.0229	0.759	(−1.758; 0.026)	Solitary	12, 14
60°	1.0	0.1403	1.509	(−1.881; 0.149)	Solitary	13, 14
60°	1.6	0.853	2.148	(−2.433; 0.701)	Oscillatory	4, 7
70°	0.4	0.0229	0.759	(−1.903; 0.024)	Oscillatory	5, 7
80°	0.4	0.0229	0.759	(−1.992; 0.022)	Oscillatory	5, 7

Before calculating the solutions in each range of Fig. 2, we consider the right-hand side of (3.10) as a function of N, i.e.

$$F(N) = \frac{\beta_0}{2}(1 - N^\gamma) + V^2\left(1 - \frac{1}{N}\right), \tag{3.15}$$

and we look for its maximum, $F(N_{\max})$, found at $N_{\max} = [2V^2/(\gamma\beta_0)]^{1/(\gamma+1)}$. Note that the function $F(N)$ has only one local extremum, namely a maximum at $N_{\max}$. The procedure of finding $F(N_{\max})$ is carried out in order to obtain an estimate for the range of possible values that the initial condition $b_z(0)$ can take. The value of the initial condition $b_z(0)$ is necessary for solving the differential equations (3.11) and (3.12). At $\xi = 0$, (3.10) reduces to

$$b_z(0)^2/2 + b_z(0)\sin\theta \leqslant F(N_{\max}) \tag{3.16}$$

since $b_y(0) = 0$ is required. Finally, setting the angle θ to a certain value and taking the already obtained values for $F(N_{\max})$ will lead to a range of possible solutions for $b_z(0)$. All calculations are performed for $\gamma = 5/3$. The set of parameters used for calculating the solutions of the stationary Sakai–Sonnerup system are summarized in Table 1.

Now, some special solutions of the system of equations (3.10)–(3.12) are presented. Because the aim here is not to discuss the complete manifold of solutions of this system of equations, only some special cases of all the solutions are presented. A detailed study of the different families of stationary solutions of the equations of the Hall magnetohydrodynamics can be found in Baumgärtel (1999), McKenzie and Doyle (2002), Stasiewicz (2004) and Mjølhus (2006). In the limit of small but finite-amplitude magnetic field fluctuations, those equations reduce to the 'derivative nonlinear Schrödinger' (DNLS) equation, which is basically nonlinear and provides solitary solutions (see, e.g., Baumgärtel 1999; Mjølhus 2006). As expected, oscillatory and solitary solutions are obtained from the system (3.10)–(3.12), and when plotted in a (b_z, b_y)-plane they appear as closed contours of different shape. Furthermore, in order to illustrate some special examples, we consider only six angles of propagation (see Table 1). The last parameter, the velocity V, can take

https://doi.org/10.1017/S0022377808007058 Published online by Cambridge University Press

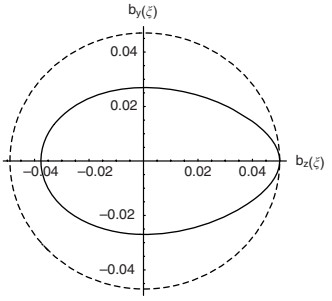


Figure 3. Oscillatory solutions ('osc. I' range) for $\theta = 30°$, $V = 0.2$, $b_z(0) = 0.05$ (dashed curve) and $\theta = 60°$, $V = 0.2$, $b_z(0) = 0.05$ (solid curve).

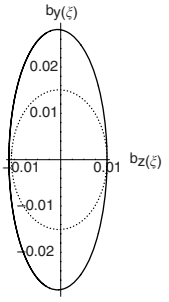


Figure 4. Oscillatory solutions ('osc. II' range) for $\theta = 10°$, $V = 0.7$, $b_z(0) = 0.01$ (dotted curve) and $\theta = 30°$, $V = 0.7$, $b_z(0) = 0.01$ (solid curve).

arbitrary positive values, which will place the solution in one of six possible ranges of solutions (see Fig. 2).

Finally, the system of equations (3.10)–(3.12), representing a nonlinear system of one algebraic and two ordinary differential equations, is solved numerically with the following initial conditions: $b_y(0) = 0$, range of $b_z(0)$, and $b_z'(0) = 0$. The solutions of the system of equations are sought inside a certain ξ-range in the form $b_y(\xi)$, $b_z(\xi)$, $|b|(\xi)$ (i.e. the magnitude of the magnetic field, $b^2(\xi) = \cos^2\theta + b_y^2(\xi) + (b_z(\xi) + \sin\theta)^2$), and $N(\xi)$. Solutions are found for different combinations of the initial conditions and the parameters $\beta_0 = 0.4$, θ and V. Another important issue is to construct a so-called 'hodograph' representation of the solutions, i.e. plotting them in a (b_z, b_y)-plane (see, e.g., Mjølhus 2006). Hence, an analogy of the visual shape of the 'hodograph' curves can be drawn to the phase curves of a mathematical pendulum in the $(\phi, \dot{\phi})$-plane, see Appendix A.

The numerical procedure is performed as follows. For each set of the input parameters (i.e. $\beta_0 = 0.4$, θ, and V) and the initial conditions (i.e. $b_y(0) = 0$, $b_z'(0) = 0$, and a value of $b_z(0)$), the system of equations (3.10)–(3.12) is solved and the solution is plotted in the (b_z, b_y)-plane. The calculation is repeated with the same set of parameters, but with another value for $b_z(0)$. Each solution corresponds to a given hodograph curve plotted in the (b_z, b_y)-plane.

3.1. Oscillatory solutions

From Fig. 2 one can recognize four ranges of oscillatory solutions. In each range, two different solutions of the Sakai–Sonnerup system are computed and plotted as hodograph curves in Figs 3–6.

https://doi.org/10.1017/S0022377808007058 Published online by Cambridge University Press

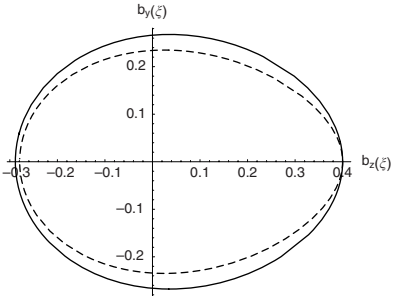


Figure 5. Oscillatory solutions ('osc. III' range) for $\theta = 30°$, $V = 1.6$, $b_z(0) = 0.4$ (solid curve) and $\theta = 60°$, $V = 1.6$, $b_z(0) = 0.4$ (dashed curve).

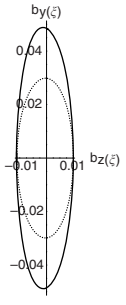


Figure 6. Oscillatory solutions ('osc. IV' range) for $\theta = 70°$, $V = 0.4$, $b_z(0) = 0.01$ (solid curve) and $\theta = 80°$, $V = 0.4$, $b_z(0) = 0.01$ (dotted curve).

From these figures, only the dependence on the angle θ can be followed in each range of oscillatory solutions. In general, the change (increase or decrease) of the angle θ lead to a change of the polarization, from nearly circular to an elliptical one. This can be seen immediately in the case of the 'osc. I' range (Fig. 3). A full parameter study, however, cannot be presented here, because we are dealing with a multi-parameter task, but we can comment on some of the characteristic dependencies of the different parameters.

The dependencies of b_y, b_z, $|b|$, and the density, N, on the coordinate ξ comprise a panel of four plots, as can be seen on Figs 7 and 8. The left panel of plots in Fig. 7 is in the range of 'osc. I', for $\beta_0 = 0.4$, $V = 0.2$, $b_z(0) = 0.05$, and for the angles $\theta = 30°$ (with dashed curve) and 60° (with solid curve). The right panel corresponds to the 'osc. II' range, with parameters $\beta_0 = 0.4$, $V = 0.7$, $b_z(0) = 0.1$, and for $\theta = 10°$ (with dotted curve) and 30° (with solid curve). The increase of the angle θ leads to an increase of the period of the oscillations in the 'osc. I' range that is reminiscent of the harmonic wave accompanied by very weak density variations in both panels. The opposite behavior is seen for the solutions in the 'osc. II' range. In the case of Fig. 7 for $\theta = 60°$ (left panel), an asymmetric shape (i.e. steepened trailing edge) of the $b_y(\xi)$ behavior becomes visible. This is a nonlinear property. The major difference while comparing both panels in Fig. 7 is the local minimum in the density N at $\xi = 0$ for the solutions in 'osc. I', i.e. the so-called local density depletion (or anticorrelation between the magnetic field and the density), in contrast to the maximum in the 'osc. II' range, i.e. local density compression (or correlation, correspondingly).

https://doi.org/10.1017/S0022377808007058 Published online by Cambridge University Press

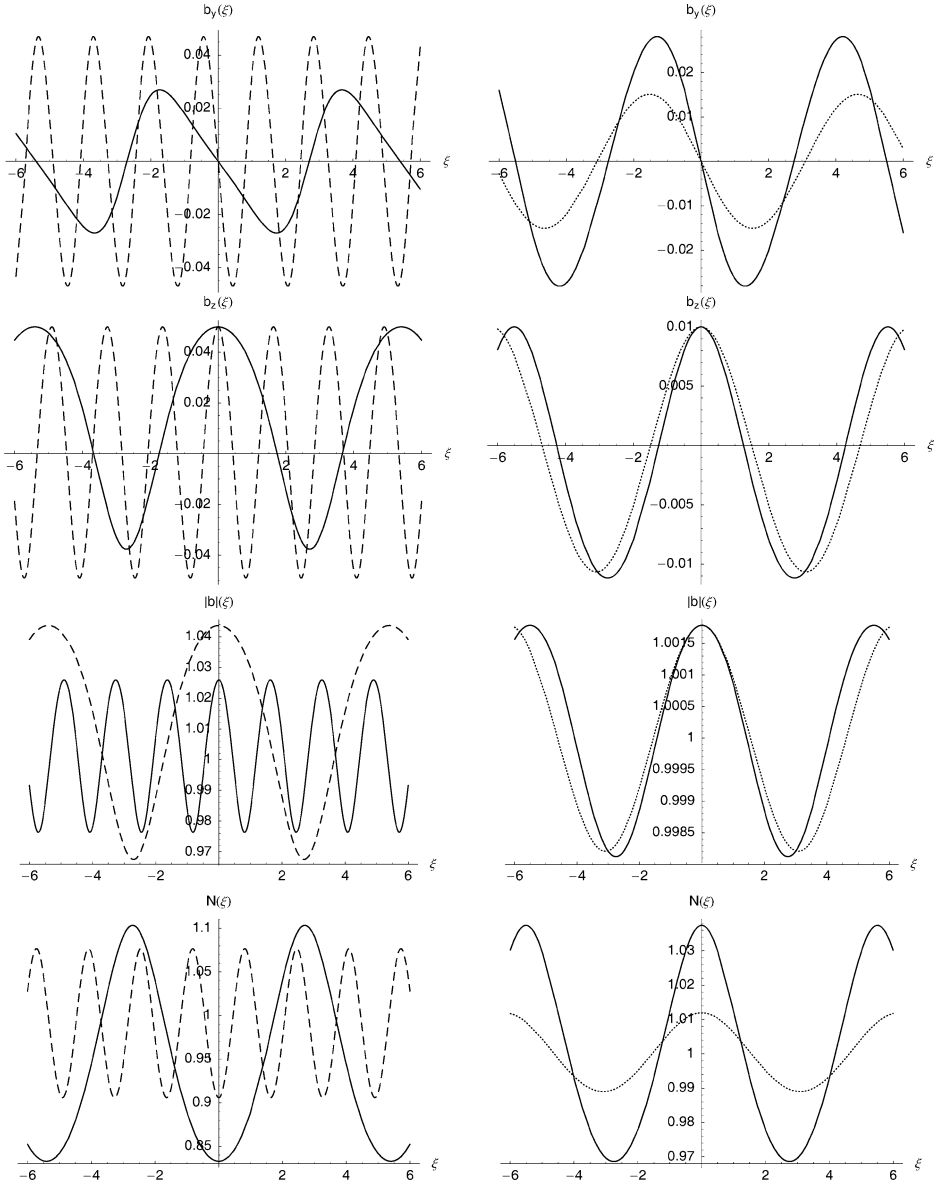


Figure 7. Plots of $b_y(\xi)$, $b_z(\xi)$, $|b|(\xi)$, and $N(\xi)$. Left panel: 'osc. I' solutions (see Fig. 3) for $\theta = 30°$, $V = 0.2$, $b_z(0) = 0.05$ (with dashed curve) and $\theta = 60°$, $V = 0.2$, $b_z(0) = 0.05$ (with solid curve). Right panel: 'osc. II' solutions (see Fig. 4) for $\theta = 10°$, $V = 0.7$, $b_z(0) = 0.01$ (with dotted curve) and $\theta = 30°$, $V = 0.7$, $b_z(0) = 0.01$ (with solid curve).

In Fig. 8 (left and right panel, correspondingly), the solutions in the ranges denoted with 'osc. III' (Fig. 5) and 'osc. IV' (Fig. 6) are presented. In this case, $V = 1.6$, $b_z(0) = 0.4$, and the angle increases from $\theta = 30°$ (solid curve) to 60° (dashed curve) in the left panel, whereas in the right panel of plots the solutions are computed for $V = 0.4$, $b_z(0) = 0.01$, and angles 70° (dotted curve) and 80° (solid curve). On this figure, correlation between the extremums of $|b|(\xi)$ and $N(\xi)$

https://doi.org/10.1017/S0022377808007058 Published online by Cambridge University Press

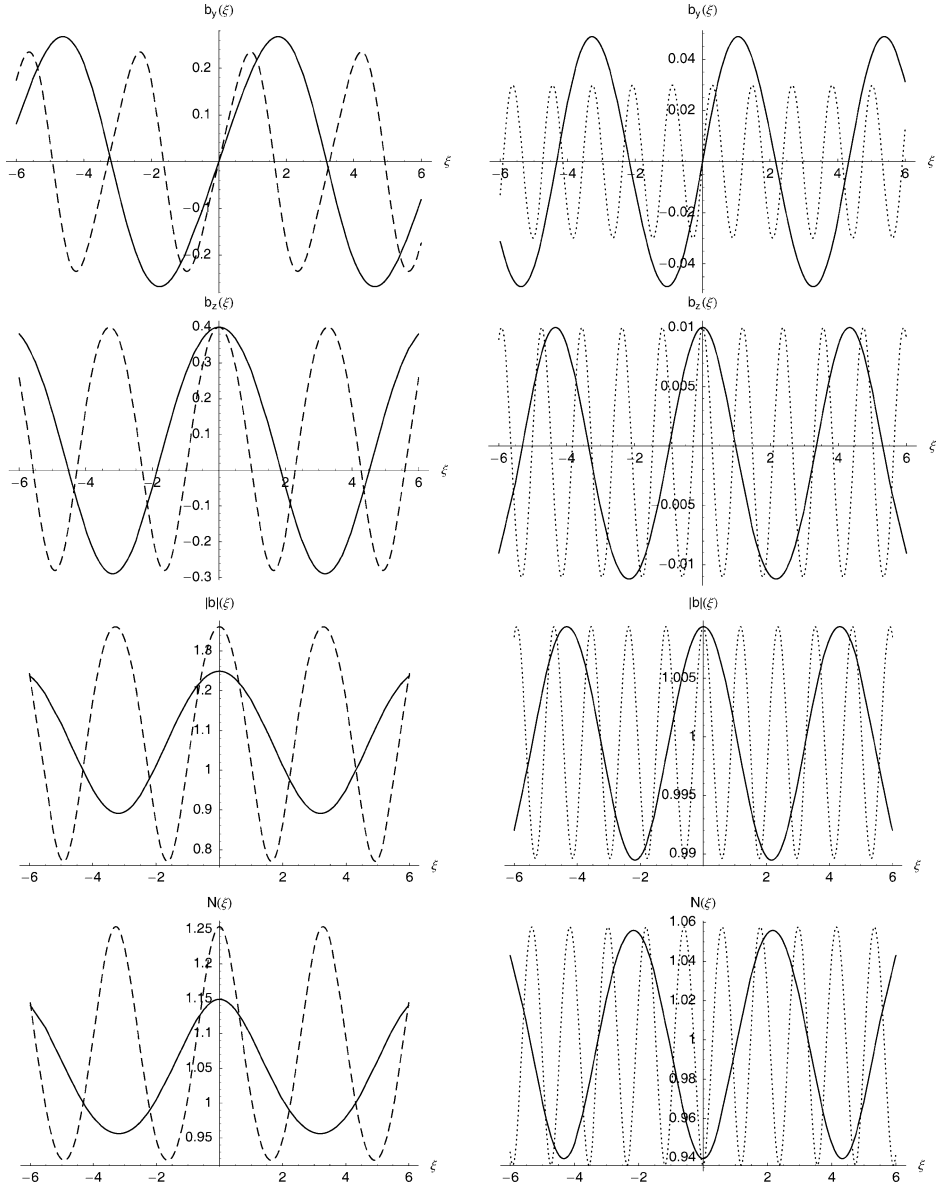


Figure 8. Plots of $b_y(\xi)$, $b_z(\xi)$, $|b|(\xi)$, and $N(\xi)$. Left panel: 'osc. III' solutions (see Fig. 5) for $\theta = 30^\circ$, $V = 1.6$, $b_z(0) = 0.4$ (with solid curve) and $\theta = 60^\circ$, $V = 1.6$, $b_z(0) = 0.4$ (with dashed curve). Right panel: 'osc. IV' solutions (see Fig. 6) for $\theta = 70^\circ$, $V = 0.4$, $b_z(0) = 0.01$ (with dotted curve) and $\theta = 80^\circ$, $V = 0.4$, $b_z(0) = 0.01$ (with solid curve).

can be seen on the left panel, i.e. in the 'osc. III' range, and anticorrelation on the right, i.e. in the 'osc. IV' range. However, if one compares the b_y-behavior (i.e. the positions of the minimum and maximum values), a difference in both 'depletion' ranges can be noticed ('osc. I' and 'osc. IV', respectively), namely, the solutions in the 'osc. I' range start with a minimum in the positive ξ-axis and *vice versa* for the oscillations in the 'osc. IV' range. The same behavior is valid for both 'compression'

https://doi.org/10.1017/S0022377808007058 Published online by Cambridge University Press

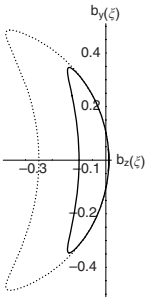


Figure 9. Arc- or banana-like solutions ('osc. II' range) for $\theta = 30°$, $V = 0.86$, $b_z(0) = -0.1$ (solid curve) and $b_z(0) = -0.25$ (dotted curve).

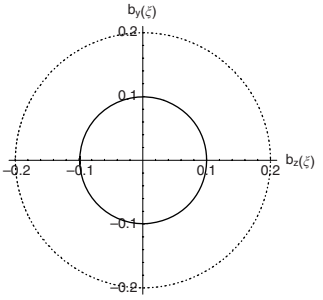


Figure 10. Nonlinear whistler solutions ('osc. III' range) for $\theta = 0°$, $V = 10$, $b_z(0) = 0.2$ (dotted curve) and $\theta = 0°$, $V = 3$, $b_z(0) = 0.1$ (solid curve).

ranges ('osc. II' and 'osc. III'), if one compares the corresponding panels in Figs 7 and 8.

The increase of the angle θ leads to an increase of the period of the oscillations in the ranges 'osc. I' and 'osc. IV', and to a decrease in the ranges 'osc. II' and 'osc. III'. Also, the amplitude of $|b|(\xi)$ in the 'osc. I' range and 'osc. III' range increases with increasing the angle θ, whereas the amplitude of $b_y(\xi)$ decreases. In the other two oscillatory ranges, 'osc. II' and 'osc. IV', the amplitude of $|b|(\xi)$ nearly does not change with such a small increase of the angle. Considering the amplitude of $b_y(\xi)$, the dependence is just the opposite than in the case of the 'osc. I' and 'osc. III' ranges, namely, an increase of the angle corresponds to an increase of the amplitude of the oscillations for the 'osc. II' and 'osc. IV' ranges.

Approaching the range of solitary solutions (i.e. moving towards the 'sol. II' range on Fig. 2) leads to the so-called 'arc'-like curves in the (b_z, b_y)-plane that can be clearly seen in Fig. 9, plotted for the set of parameters $\theta = 30°$, $V = 0.86$, and $b_z(0) = -0.1$ (solid curve) and $b_z(0) = -0.25$ (dotted curve). Such 'arc'-like (or also called 'banana'-like) polarizations are really seen in terms of magnetic field fluctuations in the interplanetary space, see Tsurutani et al. (1987a). The dependences of $b_y(\xi)$, $b_z(\xi)$, $|b|(\xi)$, and $N(\xi)$ on ξ for $b_z(0) = -0.1$ and $b_z(0) = -0.25$ are plotted in Fig. 11. In comparison to the other oscillating solutions (e.g., to the solutions in Figs 7 and 8), they have long periods of about 80–150 in the dimensionless ξ-space. Additionally, they show steepened trailing edges, where density depletions occur. Both are pure nonlinear properties.

https://doi.org/10.1017/S0022377808007058 Published online by Cambridge University Press

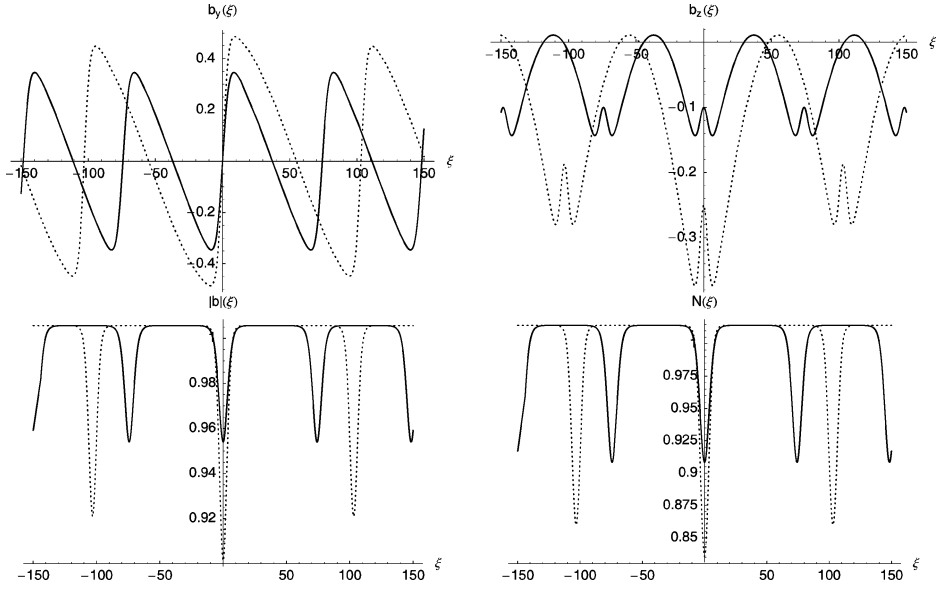


Figure 11. Plots of $b_y(\xi)$, $b_z(\xi)$, $|b|(\xi)$, and $N(\xi)$ in the case of 'osc. II'-solutions (see Fig. 9) for $\theta = 30°$, $V = 0.86$, $b_z(0) = -0.1$ (with solid) and $b_z(0) = -0.25$ (with dotted curve).

The parametric range associated with the 'osc. III' corresponds to whistler waves at low frequencies, i.e. higher than the ion-cyclotron frequency, but much lower than the electron cyclotron frequency. For these solutions, the velocity V exceeds the Alfvén speed. The hodograph curves for $\theta = 0°$, $V = 3$ and $b_z(0) = 0.1$ (solid curve) and for $\theta = 0°$, $V = 10$ and $b_z(0) = 0.2$ (dotted curve) are given in Fig. 10.

The corresponding behavior in the ξ-space is given in Fig. 12. In general, the period is decreasing with increasing V, and the associated density fluctuations become weaker with increasing V, as expected by (3.10). For $V \gg 1$, (3.10) reduces to

$$\frac{b_y^2 + b_z^2 + 2b_z \sin\theta}{2} = V^2 \frac{N-1}{N} \tag{3.17}$$

providing $|N-1| \ll 1$ for finite amplitudes, i.e. $b_y, b_z < 1$. Such whistlers are really seen in space plasmas (e.g., Gurnett 1985), and play important roles in the acceleration of electrons in the upstreaming region of shocks in collisionless plasmas (see, e.g., Miteva and Mann 2007).

Besides the increase/decrease of the angle θ, there are two other parameters that can have an influence on the shape of the oscillations, namely, the velocity V and the magnitude the initial condition $b_z(0)$ (for the range of possible $b_z(0)$ see Table 1). The dependence on a certain parameter can be clearly noticed only while the other two parameters are kept unchanged. The visualization of all dependencies would require plots for the behavior on each parameter and for each oscillatory range. That in principle can be performed, but is hardly manageable in a concise manner, since the whole manifold of solutions is broad. Hence, the main properties of the oscillatory solutions will be outlined below when the parameter V and $b_z(0)$ differ in each range of solutions.

https://doi.org/10.1017/S0022377808007058 Published online by Cambridge University Press

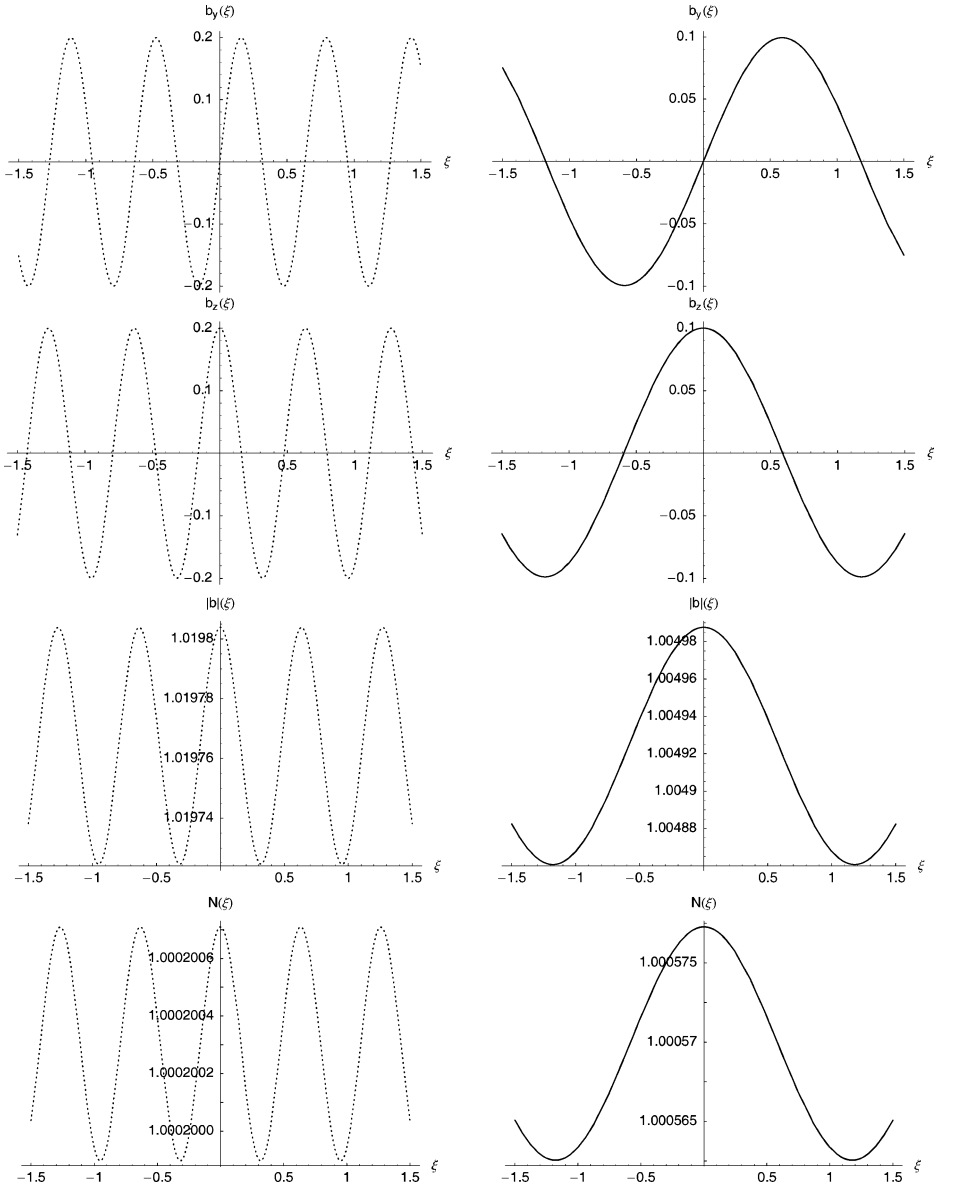


Figure 12. Plots of $b_y(\xi)$, $b_z(\xi)$, $|b|(\xi)$, and $N(\xi)$ in the case of 'osc. III' solutions (see Fig. 10). Left panel: $\theta = 0°$, $V = 10$, $b_z(0) = 0.2$. Right panel: $\theta = 0°$, $V = 3$, $b_z(0) = 0.1$.

Dependence on the velocity V:

• **'osc. I' range** for $\theta = 30°$ and $b_z(0) = 0.05$, and change of the velocity from $V = 0.2$ (see the dashed line plotted in Figs 3 and 7, left panel) to $V = 0.3$ (not given in this paper). Overall, the increase of the velocity leads to an increase of the period of the oscillations. Also, a small decrease of the amplitude in $b_y(\xi)$ and a corresponding increase in $N(\xi)$ is obtained.

• **'osc. II' range** for $\theta = 10°$ and $b_z(0) = 0.01$, and change of the velocity from $V = 0.7$ (see the dotted line plotted in Figs 4 and 7, right panel) to $V = 0.9$ (not

https://doi.org/10.1017/S0022377808007058 Published online by Cambridge University Press

given in this paper). Nearly a double increase of the period of the oscillation with the increase of the order of $\Delta V = 0.2$ is present. In contrast to the 'osc. I' range, the small increase of the amplitude of $b_y(\xi)$ corresponds to a decrease in $N(\xi)$ in the 'osc. II' range.

• **'osc. III' range** for $\theta = 60°$ and $b_z(0) = 0.4$, and change of the velocity from $V = 1.6$ (see the dashed line plotted in Figs 5 and 8, left panel) to $V = 2.0$ (not given in this paper). In this case, the increase of the velocity decreases the period of the oscillations, but increases the amplitude of the oscillations of $b_y(\xi)$ and also decreases the amplitude of $N(\xi)$ (the latter dependence was noticed in the 'osc. II' range as well).

• **'osc. IV' range** for $\theta = 80°$ and $b_z(0) = 0.01$, and change of the velocity from $V = 0.3$ (not given in this paper) to $V = 0.4$ (see the solid line plotted in Figs 5 and 8, right panel). As in the case of the 'osc. III' range, the increase of the parameter V leads to a decrease of the period of the oscillations by nearly half. Additionally, the increase with $\Delta V = 0.1$ of the velocity increases the amplitude of oscillation in the case of $b_y(\xi)$ by nearly twice and that of $N(\xi)$ by nearly one-third of the total magnitude.

Dependence on the initial condition $b_z(0)$:

• **'osc. I' range** for $\theta = 60°$, $V = 0.2$ with the initial condition changing from $b_z(0) = 0.05$ (as plotted with the solid line in Figs 3 and 7, left panel) to $b_z(0) = \pm 0.01$ (not given in this paper). When the dependencies on ξ are plotted for positive and negative values of $b_z(0)$, the extremums of the oscillations are reversed, correspondingly. Namely, for a positive value of the boundary condition, i.e. $b_z(0) = 0.01$, the oscillation starts with a minimum for b_y in the positive ξ-axis, whereas the opposite is true for $b_z(0) = -0.01$ (the oscillation starts with a maximum). This type of behavior is kept for all oscillatory ranges. As usual, the minimum/maximum of the $b_z(0)$ at $\xi = 0$ corresponds to the minimum/maximum of the $|b|$, but the minimum $|b|$ is accompanied by maximum N (density compression) for negative $b_z(0)$, and *vice versa* for a positive $b_z(0)$ (i.e. density depletion). For smaller values of $b_z(0)$, smaller periods and amplitudes of oscillations are present, but no steepening edges, as in the case of $b_z(0) = 0.05$. Thus, the nonlinear effects become prominent with the increasing values of $b_z(0)$.

• **'osc. II' range** for $\theta = 30°$, $V = 0.7$ and $b_z(0) = 0.01$ (as plotted with the solid line in Figs 4 and 7, right panel) that changes from $b_z(0) = -0.01$ to $b_z(0) = 0.02$ (not given in this paper). The amplitude and the period increase with the increasing magnitude of $b_z(0)$. In the case of positive $b_z(0)$, a maximum of $|b|$ at $\xi = 0$ corresponds to a maximum in N, whereas for a negative initial value of $b_z(0)$ the minimums of both parameters ($|b|$ and N) correlate at $\xi = 0$.

• **'osc. III' range** for $\theta = 30°$, $V = 1.6$ and $b_z(0) = 0.4$ (as plotted with the solid line in Figs 5 and 8, left panel) compared to $b_z(0) = -0.3$ and $b_z(0) = 0.8$ (not given in this paper). The dependences here are as described for the 'osc. II' range.

• **'osc. IV' range** for $\theta = 70°$, $V = 0.4$ and $b_z(0) = 0.01$ (as plotted with the dotted line in Figs 6 and 8, right panel) and also $b_z(0) = -0.01$ and $b_z(0) = 0.02$ (not given in this paper). The period of oscillation varies slightly with the change in $b_z(0)$, but the amplitude increases with the increase of the magnitude of $b_z(0)$. In contrast to the 'osc. II' and 'osc. III' ranges, in the 'osc. IV' range for $b_z(0) > 0$

https://doi.org/10.1017/S0022377808007058 Published online by Cambridge University Press

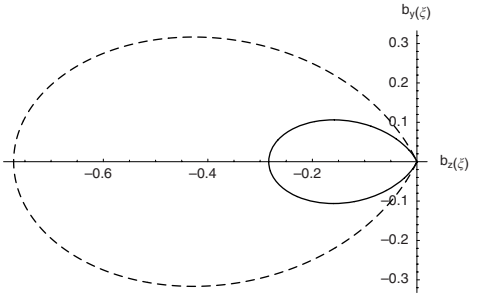


Figure 13. Solitary solutions ('sol. I' range) for $\theta = 30°$, $V = 0.55$ (solid curve) and $\theta = 60°$, $V = 0.4$ (dashed curve).

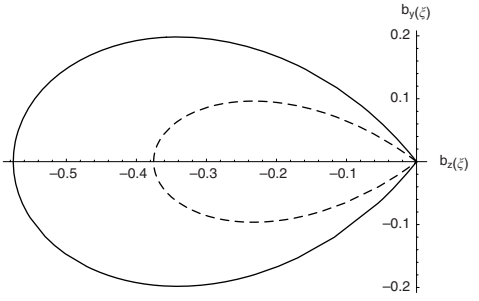


Figure 14. Solitary solutions ('sol. II' range) for $\theta = 30°$, $V = 1.0$ (solid curve) and $\theta = 60°$, $V = 1.0$ (dashed curve).

a maximum of $|b|$ at $\xi = 0$ corresponds to a minimum in N, and for $b_z(0) < 0$ a minimum of $|b|$ at $\xi = 0$ corresponds to a maximum in N.

3.2. Solitary solutions

In the range of parameters corresponding to the areas of 'sol. I' and 'sol. II' (see Fig. 2), solitary solutions are obtained, as depicted on the 'hodographs' in Fig. 13 ('sol. I') and in Fig. 14 ('sol. II'). The corresponding explicit solutions are presented in Fig. 15. In all the presented cases, $b_z(\xi)$ and $|b|(\xi)$ are always smaller than 0 and 1, respectively. For the parameters related to the 'sol. I' range, the solitons are accompanied by a density compression. A density depletion occurs for the solitary solutions in the parameter range 'sol. II'. Such solutions are found as so-called magnetic holes in the interplanetary space (see, for instance, Baumgärtel 1999; Stasiewicz 2004).

Additionally, the overall shape of the oscillatory and the solitary solutions intrinsically differs as a function of ξ. From (3.11), it follows that an extremum of b_z (i.e. $db_z/d\xi = 0$) corresponds to $b_y = 0$ in the specific case of b_z^{extr}. An analytical expression for the value of b_z in the point of the extremum can be found by setting the condition $b_y = 0$ in (3.10), or finally

$$b_z^{\mathrm{extr}} = \sin\theta \pm \sqrt{\sin^2\theta + 2F(N)}. \tag{3.18}$$

This can be seen by comparing the numerical solutions for the oscillatory solutions (Figs 7 and 8), having a maximum of b_z at $\xi = 0$, whereas in the solitary case

https://doi.org/10.1017/S0022377808007058 Published online by Cambridge University Press

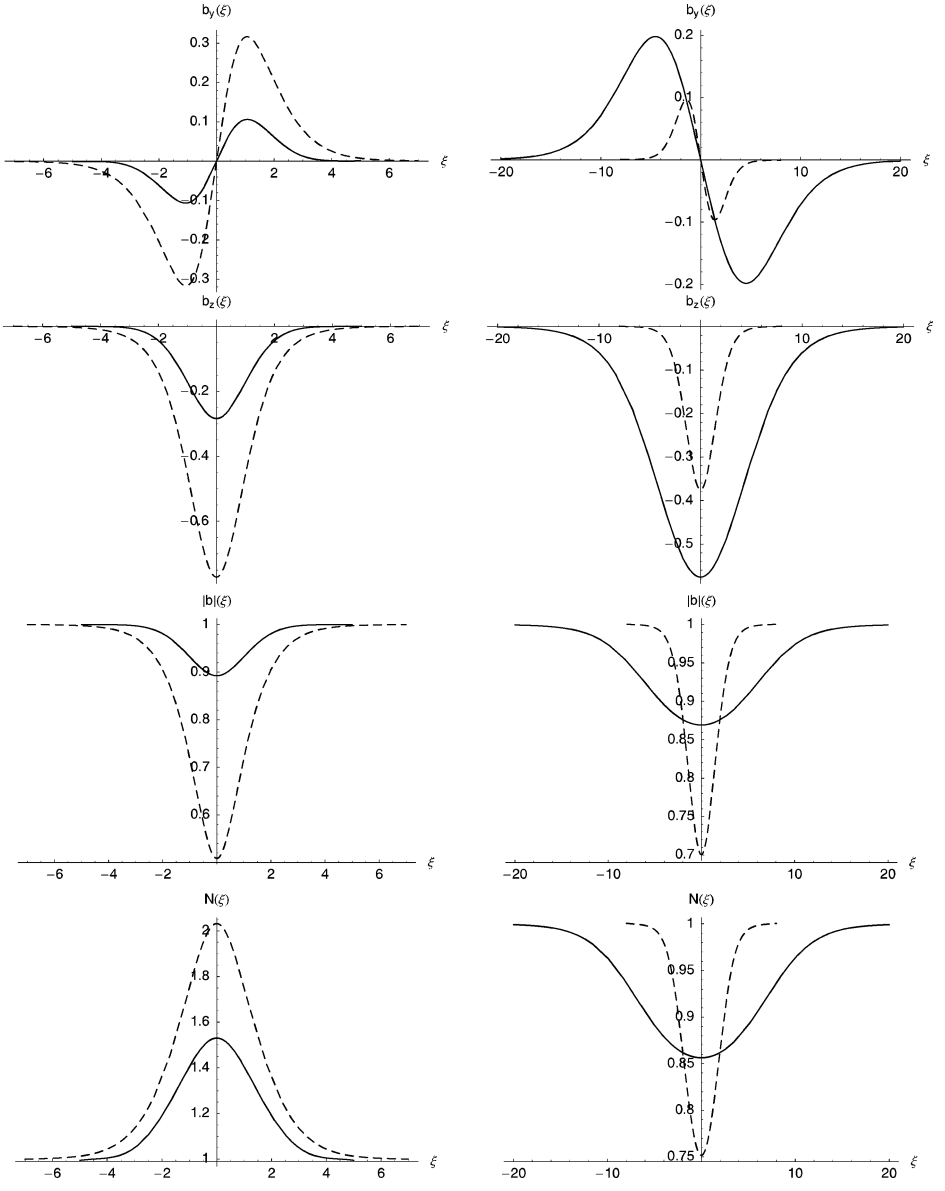


Figure 15. Plots of $b_y(\xi)$, $b_z(\xi)$, $|b|(\xi)$, and $N(\xi)$. Left panel: 'sol. I' solutions (see Fig. 13) for $\theta = 30°$, $V = 0.55$, $b_z(0) = -0.2835$ (with solid curve) and $\theta = 60°$, $V = 0.4$, $b_z(0) = -0.7716$ (with dashed curve). Right panel: 'sol. II' solutions (see Fig. 14) for $\theta = 30°$, $V = 1.0$, $b_z(0) = -0.5758$ (with solid curve) and $\theta = 60°$, $V = 1.0$, $b_z(0) = -0.3754$ (with dashed curve).

in Fig. 15, b_z has a minimum at $\xi = 0$. The density compression (the maximum of $N(\xi = 0)$) is obtained in the 'sol. I' range (as in the 'osc. II' and 'osc. III' ranges), whereas the density depletion (the minimum of $N(\xi = 0)$) occurs in the 'sol. II' range (and also in the 'osc. I' and 'osc. IV' ranges). In all plots, $b_y(\xi = 0) = 0$, as required from the initial condition.

https://doi.org/10.1017/S0022377808007058 Published online by Cambridge University Press

The solitary solutions presented here were obtained for a certain special value of the initial condition $b_z(0)$ in any of the solitary ranges (for example compare with the unique value for the solitary solution in the case of a mathematical pendulum, see Appendix A). Although presenting a full parameter dependence is very difficult in the solitary ranges, Fig. 15 (right panel) gives some trends of the general behavior for the same parameter V and for increasing angle θ (from 30° to 60°). Namely, the width of the solitary structure decreases with increasing angle. The amplitude of $b_y(\xi)$ and $b_z(\xi)$ also decrease, whereas the amplitude of $|b|(\xi)$ and $N(\xi)$ increase with increase of the angle, for the solitary solutions in the 'sol. II' range. A similar comparison cannot be performed for the 'sol. I' range, because all parameters are different, but one can see the overall behavior of the solutions in this range, i.e. increasing width and amplitude with increasing angle θ and decreasing velocity V.

4. Conclusions

The Sakai–Sonnerup system (3.10)–(3.12) describes the evolution of one-dimensional plasma waves for frequencies much lower than the electron cyclotron frequency, so that the displacement current and the charge separation effects can be neglected. The stationary solutions of the Sakai–Sonnerup system offers both oscillatory and solitary solutions, reminiscent of the fully nonlinear motion of a mathematical pendulum. In this respect, the solitary solution separates different types of solutions as was discussed in the previous subsection. It should be pointed out that the solitary solution is related to a very special choice of parameters and initial conditions. This fact means actually that the oscillatory (or periodic) solutions are mostly probable to occur in space plasmas. They are related to different kinds of polarization, e.g. circular, elliptical and arc-like polarization, as really observed in terms of low-frequency magnetic field fluctuations in space plasmas. In summary, the following dependencies are noticed for a positive value of the boundary condition $b_z(0)$, i.e. $b_z(0) > 0$:

- $|b|$-maximum – $N(\xi)$-maximum (correlation): 'osc. II', 'osc. III';
- $|b|$-maximum – $N(\xi)$-minimum (anticorrelation): 'osc. I'; 'osc. IV'.

When $b_z(0)$ has a negative initial value, i.e. $b_z(0) < 0$, there is only a minimum of $|b|$ at $\xi = 0$, and finally the above relationships reduce to:

- $|b|$-minimum – $N(\xi)$-minimum (correlation): 'osc. II', 'osc. III', 'sol. I';
- $|b|$-minimum – $N(\xi)$-maximum (anticorrelation): 'osc. I', 'osc. IV', 'sol. II'.

The oscillations in the ranges 'osc. I' and 'osc. IV' display similar behavior. The same could be noticed for the ranges 'osc. II' and 'osc. III'. However, only a small part of all possible solutions of the Sakai–Sonnerup system of equations was investigated. Nevertheless, some typical dependencies in each range of solutions for $b_y(\xi)$, $b_z(\xi)$, $|b|(\xi)$, $N(\xi)$ on the parameters θ, V, and $b_z(0)$ were presented.

Acknowledgement

R.M. was supported by DRL grant No. 50/QL/0001.

Appendix A. Example of mathematical pendulum

We look at the 'mathematical pendulum' in order to illustrate the nature of 'oscillatory' and 'solitary' solutions. The movement of a mathematical pendulum with the length l is usually described by $d^2\phi/dt^2 + \omega_0^2 \sin\phi = 0$, with $\omega_0 = (g/l)^{1/2}$

https://doi.org/10.1017/S0022377808007058 Published online by Cambridge University Press

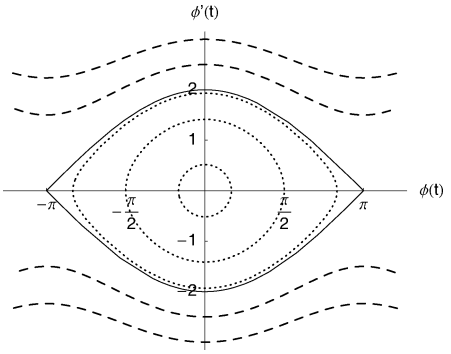


Figure A.1. Phase portrait of a mathematical pendulum.

and g the gravitational acceleration. The angle ϕ denotes the temporal deflection of the pendulum off the vertical axis. Normalizing the time t to the inverse of the frequency ω_0, i.e. $t' = t\omega_0$, the equation above reduces to $d^2\phi/dt'^2 + \sin\phi = 0$, where the primes denote the normalized quantities but will be omitted further on. In order to solve directly this normalized equation, one needs to set two initial conditions. To obtain the oscillatory solutions of the pendulum, one sets $\phi(t = 0) = \phi_0$ and $\dot{\phi}(t = 0) = 0$. Then, ϕ_0 denotes the amplitude of the oscillations. The initial angle of deflection of the pendulum ϕ_0 can take any value in the range 0–π, but here for illustration we chose $\phi_0 = 30°$, $90°$, and $150°$. Such a choice of the initial conditions will result in the concentric curves in the $(\phi, \dot{\phi})$-plane, plotted with a dotted line in Fig. A.1.

However, at one special point, namely $\phi_0 = \pi$, the only possible solitary solution is obtained (this is the separatrix, plotted with the solid line in Fig. A.1). For the rotational motion, which is also possible for a mathematical pendulum, the initial conditions need to be changed (in this case to $\phi(t = 0) = 0$ and $\dot{\phi}(t = 0)$ with values ± 2.5 and ± 3 and plotted with the dashed line in Fig. A.1). Note that both the 'oscillatory' and 'rotational' solutions are periodic and a 'solitary' solution occurs only for a single (definite) value of the initial conditions. In the case of the 'solitary' solution, the movement starts with $\dot{\phi}(t = 0) = 0$ at $\phi(t = 0) = \pi$ and needs an infinite time to reach $\phi = -\pi$.

Multiplying the normalized equation of the mathematical pendulum by $\dot{\phi}$ and, subsequently, integrating once, one gets $\dot{\phi} = \pm\sqrt{2(C + \cos\phi)}$, where C is the integration constant. In order to get a real solution, $C + \cos\phi \geqslant 0$ is required. Then, the three types of solutions are obtained with the following choice for C.

(*a*) $-1 < C < 1$ leads to an 'oscillatory' solution (see the dotted curves enclosed by the solid curve in Fig. A.1). Then, $\phi_{\max} = \arccos(-C) < \pi$ gives the amplitude of the oscillations.

(*b*) $C = 1$ provides the 'solitary' solution (see the solid curve in Fig. A.1). Here, the movement starts at $\phi = \pi$ at $t = 0$ and needs an infinite time to reach the final point at $\phi = -\pi$.

(*c*) $C > 1$ provides no zeros of $\dot{\phi}$, i.e. it leads to 'rotational' solutions. Here, $C = 2.125$ (corresponding to $\dot{\phi}(0) = \pm 2.5$), and $C = 3.5$ ($\dot{\phi}(0) = \pm 3$) are chosen both for $\phi(0) = 0$ (see the dashed curves in Fig. A.1).

https://doi.org/10.1017/S0022377808007058 Published online by Cambridge University Press

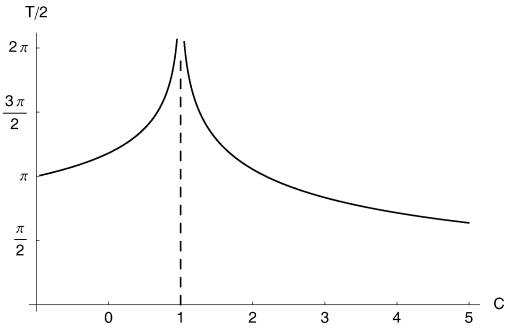


Figure A.2. Dependence of the half period of the pendulum on the constant C.

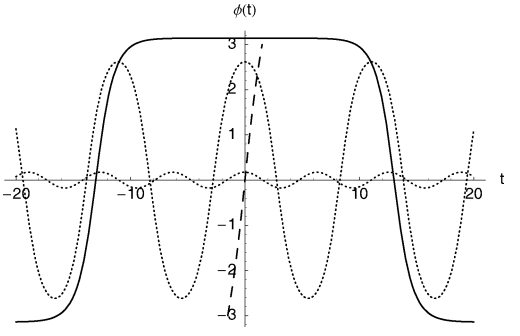


Figure A.3. Plot of $\phi(t)$, where $\phi(0) = 10°$, $\phi(0) = 150°$ are denoted with dotted, $\phi(0) = \pi$ with solid and $\dot{\phi}(0) = 2.5$ with the steep dashed curves.

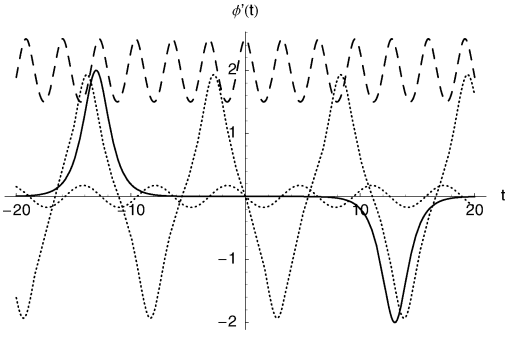


Figure A.4. Plot of $\dot{\phi}(t)$, where $\phi(0) = 10°$, $\phi(0) = 150°$ are denoted with dotted, $\phi_0 = \pi$ with solid and $\dot{\phi}(0) = 2.5$ with dashed curves.

In Figs A.3 and A.4, the dependences of $\phi(t)$ and $\dot{\phi}(t)$ for four different initial conditions are shown. Some of the solutions/curves from Fig. A.1 are given in both figures, namely, two oscillatory solutions (for $\phi(0) = 10°$ and $\phi(0) = 150°$), the separatrix/solitary solution (for $\phi(0) = \pi$) and one rotational solution (for $\dot{\phi}(0) = 2.5$). Also, one can follow the change in the shape of the curves, while passing from one type of solution (e.g., oscillatory/solitary) to another (e.g., solitary/rotational), correspondingly. The period increases with an increase of the amplitude for

https://doi.org/10.1017/S0022377808007058 Published online by Cambridge University Press

$\phi(0) < \pi$, whereas it decreased after exceeding $\phi(0) = \pi$ (see Fig. A.2). The solitary nature of the solution with $\phi(0) = \pi$ is obvious (compare the angles near π).

The mathematical pendulum is a simple, but non-trivial example of a fully nonlinear problem. For small deflections, one obtains linear oscillations with a frequency that is not dependent on the amplitude. With increasing amplitudes, the motion leaves the linear regime. This is characterized by the fact that the period of the oscillation becomes dependent on the amplitude. The study performed here shows that the period increases with amplitude (see Figs A.2 and A.3). If the amplitude reaches π, one gets a very special solution, which corresponds to the solitary one. Here, the pendulum starts with an infinitely slow velocity at π and reaches asymptotically the state $-\pi$ after a infinitely long time, i.e. $T/2 \to \infty$ (Fig. A.2). This solitary solution separates the oscillatory solutions from the rotational ones (Fig. A.1). All solutions can be characterized by the initial conditions, i.e. the choice of $\dot{\phi}$ and C, covering the ranges $0 \leqslant \dot{\phi} < \infty$ and $-1 \leqslant C < \infty$, respectively. It should be noted that the solitary solution is only given for one point in this parameter range, i.e. $\dot{\phi} = 0$ and $C = 1$. All other conditions provide periodic (either oscillatory or rotational) solutions. This impressively demonstrates the singular nature of the solitary solution.

References

Akimoto, K., Winske, D., Onsager, T. G., Thomsen, M. F. and Gary, S. P. 1991 Steepening of parallel propagating hydromagnetic waves into magnetic pulsations – a simulation study. *J. Geophys. Res.* **96**, 17 599–17 607.

Baumgärtel, K. 1999 Soliton approach to magnetic holes. *J. Geophys. Res.* **104**, 28 295–28 308.

Fairfield, D. H. and Behannon, K. W. 1976 Bow shock and magnetosheath waves at Mercury. *J. Geophys. Res.* **81**, 3897–3906.

Goldstein, M. L., Smith, C. W. and Matthaeus, W. H. 1983 Large amplitude MHD waves upstream of the Jovian bow shock. *J. Geophys. Res.* **88**, 9989–9999.

Gurnett, D. A. 1985 *Plasma Waves and Instabilities (Geophysical Monograph Series, 35)*. Washington DC: American Geophysical Union, pp. 207–224.

Hoppe, M. and Russell, C. T. 1981 On the nature of ULF waves upstream of planetary bow shocks. *Adv. Space Res.* **1**, 327–332.

Hoppe, M. and Russell, C. T. 1983 Plasma rest frame frequencies and polarizations of the low-frequency upstream waves—ISEE 1 and 2 observations. *J. Geophys. Res.* **88**, 2021–2027.

Hoppe, M. M., Russell, C. T., Frank, L. A., Eastman, T. E. and Greenstadt, E. W. 1981 Upstream hydromagnetic waves and their association with backstreaming ion populations—ISEE 1 and 2 observations. *J. Geophys. Res.* **86**, 4471–4492.

Huba, J. D. 1995 Hall magnetohydrodynamics in space and laboratory plasmas. *Phys. Plasmas* **2**, 2504–2513.

Mann, G. and Lühr, H. 1991 Comparison of low frequency magnetic field fluctuations upstream of earth's bow shock with a strong Alfvénic turbulence model. *Ann. Geophys.* **9**, 681–689.

Mann, G., Lühr, H. and Baumjohann, W. 1994 Statistical analysis of short large-amplitude magnetic field structures in the vicinity of the quasi-parallel bow shock. *J. Geophys. Res.* **99**, 13 315–13 323.

McKenzie, J. F. and Doyle, T. B. 2002 The properties of fast and slow oblique solitons in a magnetized plasma. *Phys. Plasmas* **9**, 55–63.

Mjølhus, E. 2006 Velocity–amplitude relationships and polarizations in families of MHD solitary waves. *Phys. Scr.* T **122**, 135–153.

https://doi.org/10.1017/S0022377808007058 Published online by Cambridge University Press

Miteva, R. and Mann, G. 2007 On the electron acceleration at shock waves in the solar corona. *Astron. Astrophys.* **474**, 617–625.

Paschmann, G., Sckopke, N., Bame, S. J., Asbridge, J. R., Gosling, J. T., Russell, C. T. and Greenstadt, E. W. 1979 Association of low-frequency waves with suprathermal ions in the upstream solar wind. *J. Geophys. Res.* **6**, 209–212.

Riedler, W., Schwingenschuh, K., Yeroshenko, Y. G., Styashkin, V. A. and Russell, C. T. 1986 Magnetic field observations in Comet Halley's coma. *Nature* **321**, 288–289.

Sakai, J.-I. and Sonnerup, U. O. 1983 Modulational instability of finite amplitude dispersive Alfvén waves. *J. Geophys. Res.* **88**, 9069–9079.

Scholer, M. 1993 Upstream waves, shocklets, short large-amplitude magnetic structures and the cyclic behavior of oblique quasi-parallel collisionless shocks. *J. Geophys. Res.* **98**, 47–57.

Scholer, M., Trattner, K. J. and Kucharek, H. 1992 Ion injection and Fermi acceleration at earth's bow shock—the 1984 September 12 event revisited. *Astrophys. J.* **395**, 675–681.

Schwartz, S. J. and Burgess, D. 1991 Quasi-parallel shocks—a patchwork of three-dimensional structures. *Geophys. Res. Lett.* **18**, 373–376.

Stasiewicz, K. 2004 Theory and observations of slow-mode solitons in space plasmas. *Phys. Rev. Lett.* **93**, 125 004(1–4).

Tsurutani, B. T., Brinca, A. L., Smith, E. J., Thorne, R. M., Scarfe, F. L., Gosling, J. T. and Ipavich, F. M. 1987a Magnetohydrodynamic waves detected by ice at distances equal-to 280,000,000-kilometers from comet p/Halley—cometary or solar wind origin. *Astron. Astrophys.* **187**, 97–102.

Tsurutani, B. T., Smith, E. J., Thorne, R. M., Gosling, J. T. and Matsumoto, H. 1987b Steepened magnetosonic waves at Comet Giacobini-Zinner. *J. Geophys. Res.* **92**, 11 074–11 082.

Tsurutani, B. T., Ho, C. M., Arballo, J. K., Goldstein, B. E. and Balogh, A. 1995 Large amplitude IMF fluctuations in corotating interaction regions: Ulysses at midlatitudes. *Geophys. Res. Lett.* **22**, 3397–3400.

https://doi.org/10.1017/S0022377808007058 Published online by Cambridge University Press